SEPARATION CONTROL BY A MICROFABRICATED SDBD PLASMA ACTUATOR FOR SMALL ENGINE TURBINE APPLICATIONS: INFLUENCE OF THE EXCITATION WAVEFORM

E. Pescini[a, 1], M.G. De Giorgi[a], A. Suma[a], L. Francioso[b], A. Ficarella[a]
[a] Department of Engineering for Innovation, University of Salento, Via Monteroni, Lecce-Italy
[b] Institute for Microelectronics and Microsystems - CNR–IMM, Via Monteroni, Lecce-Italy

1 Abstract

Small engines will be finding increasing applications in unmanned aerial vehicles (UAVs), drones and helicopters. However, their turbomachines exhibit lower efficiencies than those of large scale engines. In this context, the aerodynamic losses in the low-pressure turbines (LPTs) are largely accountable to flow separation at low Reynolds numbers operation, i.e. in cruise conditions. Active flow control is a promising technology to suppress separation, thus reducing losses, fuel consumption rates and therefore emissions.

The present paper is focused on the experimental investigation of the potentialities of a Single Dielectric Barrier Discharge Plasma Actuator (SDBDPA) to reattach the separated flow at a Reynolds number of $2 \cdot 10^4$. The influence of the high voltage (HV) waveform supplying the SDBDPA on both flow separation control and device power dissipation was studied.

The investigated SDBDPA was manufactured by microfabrication techniques. Photolithography ensured thin metal deposition with high manufacturing reliability control. Due to the possible device degradation during operation, emphasis was put in selecting thin film materials that could withstand the plasma environment. Schott alkali-free borosilicate glass substrate was chosen as dielectric, while a multilayer tungsten (W)/titanium nitride (TiN) as electrode material.

The experimental approach comprised the actuator testing over a curved wall plate, designed with a shape to reproduce the suction surface of a LPT and installed in closed loop wind tunnel test section. The SDBDPA was located at the front side of the adverse pressure gradient area, in order to control flow separation.

Different HV excitation waveforms (sinus, triangle and square) and amplitudes were tested and compared, aiming to identify the input signal that gave the best flow control authority and device energy conversion efficiency. The applied voltage and the discharge current were acquired in order to determine the actuator dissipated power. Two-dimensional (2-D) flow velocity measurements were carried out by laser Doppler velocimetry (LDV) and particle image velocimetry (PIV).

Velocity results showed that the extension of the separation area was reduced by actuation. Moreover, when the actuator was on, the boundary layer thickness and the negative velocity magnitude decreased. Their reduction increased with the applied voltage (i.e. higher power dissipations). At comparable peak-to-peak applied voltages, the sinus waveforms slightly outperformed the other waveforms; however, while the sinus and triangle ones had comparable power dissipation, the square wave always dissipated the most.

Keywords: low pressure gas turbine, low Reynolds number, active flow control, dielectric barrier discharge plasma actuator, microfabrication, high voltage waveform.

2 Introduction

Aeronautical LPT blades might be subjugated to low Reynolds number flow effects due to the change in density from high altitude operation. In this circumstance, the Reynolds number can decrease below 25000. Laminar separation may thus develop on the suction surface together with the appearance of secondary flows [1], with a subsequent drop in the engine performance. The low Reynolds condition becomes even a greater issue when dealing with modern high-lift blades [2] and small/medium-sized gas turbines [3]–[7]. Because of the reduced size, small LPTs, used or planned to be used in small aircrafts, UAVs and drones, exhibit not only low-Reynolds numbers but also low flow rates, low component pressure ratios and high rotational speed, which lead to a further reduction in efficiency in comparison with larger size machines [5]–[7]. Counteract flow separation is thus of crucial importance.

Laminar flow separation was experimentally [3] and numerically [8] observed in a single stage axial-flow turbine, operating at a Reynolds number (based on the stator chord length and stator inlet velocity) equal to 20.000 and an inlet turbulence intensity of 0.5%. Moreover, it was also found a strong interaction of the separated flow with the secondary flows. Similar experimental investigations and findings under the same operating conditions are also found in Matsunuma *et al*. [9]. Secondary flows usually cause almost 30-50% of the overall loss in a blade row with a significant reduction of the LPT efficiency [10]. A nearly 300% increase in the loss coefficient was indicated for an aero-engine LPT at a Reynolds number below $2 \cdot 10^5$, primarily associated with a laminar separation over the trailing half of the blade suction surface [11].

[1] Address all correspondence to this author

The control of laminar separation bubbles has been subject of many studies in recent years. Several flow control techniques have been investigated with particular interest in active flow control methods [12]–[16].
Among active flow control devices, an interesting one is the SDBDPA, which is cheap, easy to be implemented on a surface, light in weight and high response frequency. Moreover, it is powered with an electrical input energy that allows easy control and high-bandwidth modulation of the actuation. The SDBDPAs are composed of two metallic electrodes separated by a dielectric layer: one electrode is supplied with a HV waveform and exposed to the surrounding flow; the other one is grounded and covered by insulating material. The application a voltage waveform in the kV and kHz ranges (with or without modulation or pulsing) causes the air near the plasma actuator to weakly ionize. The electric field interaction with the charged particles results in a net body force that acts on the neutrally charged air. When operating in a separated flow, the body force effect leads to the energization of the boundary layer, which can result in its reattachment.
Plasma actuators have been already investigated as an effective active control strategy in eliminating the LPT separation at low Reynolds numbers [1], [11], [15]–[19]. Figure 1 shows a conceptual drawing on SDBDPAs applied on the suction surface of LPT rotor blades. The actuators, placed approximately at the separation location, bring to flow reattachment. However, it is important to mention that these devices possess low electrical-to-fluidic energy conversion efficiency and the effect that the external flow has on the performance of the actuator itself must also be considered [15], [20]–[22]. For this reason, they have primarily been limited to relatively low speed (freestream velocities lower than 30 m/s) and low Reynolds number (of maximum a few 10^5) [23], [24]. Nevertheless, claims of control authority for freestream velocities as high as 60 m/s with Reynolds number of 10^6 have been presented in the literature [25], [26]. Among the parameters improving the effectiveness of the SDBDPAs, it is established that changes in the geometry of the actuator (dielectric layer material [27], [28], thickness of the both the dielectric layer [27], [28] and exposed electrode [29], electrode gap [28], grounded electrode width and number [30], [31]), in the dielectric layer surface temperature [32] and in the electrical settings [26]–[28], [33]–[41] can be effective to significantly enhance electric wind velocity and, consequently, the resulting force production. Moreover, multiple actuator arrays could be adopted [27], [28]. However, the cost implications in terms of dissipated power should be always evaluated.
In Bernard and Moreau [37], the influence of the HV waveform was experimentally investigated for four different signals (sine, square, positive and negative ramps) supplying a SDBDPA placed in initially quiescent flow conditions. Results showed that, if one wants to optimally use the SDBDPAs in terms of mean force by electrical power consumption, the sine waveform is recommended as input voltage. Indeed, at a constant consumed electrical power, a sine waveform gave the best performance. Nevertheless, at constant applied voltage or frequency, the square signal caused higher thrust, but at a price of a large consumed power. A second metric that determines the effectiveness of such actuator for control is the mean velocity of the electric wind produced by the plasma, as well as the amplitude of the velocity fluctuations that can be achieved. Always in Bernard and Moreau [37], the largest mean flow velocity, at constant applied voltage and frequency, was observed for a square input waveform; this agrees with the force measurements. The sine waveform led to a slightly smaller mean flow velocity when performances were further degraded by using the ramp shapes (especially the positive one). However, the largest fluctuations in the velocity component in the horizontal direction (i.e., direction of the plasma layer) are observed for a sine waveform when they are minimized by using a positive ramp. This suggested that sine waveform could be probably more effective in flow separation control. Again, the amplitude of vertical velocity fluctuations was increased by using a sine waveform.
In Jolibois and Moreau [38], the waveform of the applied voltage (sine, triangle, square, trapezium, positive and negative ramps) has also been investigated experimentally as input parameter able to influence the actuator electromechanical performance. Experimental tests were always performed in absence of external airflow. Results showed that at same electrical power consumption, the discharge induced the same maximum velocity whatever the waveform, excepted with the square and the positive ramp ones that resulted in a smaller electric wind velocity. Comparing the sinus and square waveforms, it was found that, at similar power consumption, the sine voltage induced a faster electric wind with a discharge closer to the wall than the square waveform. This might be explained by the fact that, for example, a voltage of 18 kV was needed to consume 0.75 W/cm with the sine HV whereas only 16 kV were necessary in the case of the square high voltage.

The aim of this paper was to investigate the influence of the HV waveform supplying a SDBDPA on flow separation control in a LPT at low Reynolds number. Therefore, differently from the available literature studying the role of the electric waveform (where the actuator was always placed in a quiescent flow [27], [37]–[39]), in the present work experiments were conducted in presence of external flow. Three different excitation signals (sine, square and triangle) were experimentally tested at fixed frequency and different amplitudes. The LPT rotor blade investigated in the works of Matsunuma *et al.* [1], [9], [42], [43] was considered. 2-D flow velocity measurements in presence of actuation were carried out by PIV. Simultaneously, the SDBDPA applied voltage and the discharge current flowing in the circuit were acquired in order to determine the device dissipated power. Velocity measurements in absence of actuation were also performed by PIV and LDV.
The SDBDPA materials and manufacturing procedure were carefully chosen, both influencing the actuator durability [44], [45].
Dielectric materials to be used in SDBD plasma actuator applications must possess a high dielectric strength and must not chemically degrade in the presence of the plasma [27]. In many studies concerning flow control aspects, polymers have been used as dielectric [23]. The advantage of those materials is their relative simplicity of use. On the other hand, they may not withstand the intense bombardment of ions, radical species, or ultraviolet radiations, which are emitted by plasma filaments [28], [46], [47]. A commonly used dielectric is the Kapton polyimide film; however, it is known to be susceptible to oxidative degradation, so it can be damaged over time in the presence of ionized air. Hanson et al. [48] showed that for an increasing number of Kapton tape layers, the relative changes in the actuator electrical properties over time (due to dielectric degradation) reduced; however the dielectric thickness always reduced by removal of the top exposed Kapton layer. In Rigid et al. [47], a glass-reinforced epoxy laminate sheet dielectric was

investigated by scanning electron microscope (SEM) and charged coupled device (CCD) images. Results revealed that the degradation on the actuator was subjected to a failure rate that increased with the cumulative time of plasma operation and the magnitude of supplied voltage. In Pons et al. [4], optical microscope images of the surface degradation for polymethyl methacrylate and polyvinyl chloride were shown. They were compared with a borosilicate glass exposed to the same discharge conditions and which exhibited no observable degradation. In Houser et al. [45] thin alkali-free borosilicate glass (ranging from 200 µm to 500 µm thick) was chosen as a dielectric for reasons of compatibility with microfabrication processing and dielectric properties preferable to basic borosilicate glasses. The same material (300 µm thick) was chosen in Pescini et al. [44]. In both works, SEM analyses showed no obvious signs of dielectric degradation.

Together with the dielectric material choice, particular attention was paid in the selection of the electrode material, as it could oxidize in the high corrosive plasma environment. Pescini et al. [44] investigated the gold electrodes resistance, by both SEM images and energy dispersive X-ray spectroscopy (EDS) analysis. After usage, unexpected degradation effects were observed on both the front side and back side of the actuator electrodes. Similar investigations were performed by Houser et al. [45] on copper and W electrodes. The results showed that while copper exposed electrode exhibited appreciable degradation along the plasma-forming edge after usage, the W one presented limited degradation. Moreover, it was found that the electrode material, due to the degradation pattern, highly influences the plasma regime; while tungsten electrodes showed uniform plasma generation, copper electrodes caused filamentary discharges, which in turn could lead to irregularities in the induced flow and localized stresses on the device, bringing to premature failure.

For all the aforementioned reasons, an opportune choice of the DBD material has to be done or suitable treatments/coatings have to be applied to reduce the surface degradation.

Therefore, in the light of the literature works findings, thin Schott AF-32 alkali-free borosilicate glass dielectric material was here selected onto which W electrodes were deposited. Aiming to develop efficient, reproducible and durable devices, optical lithography fabrication technique was adopted. Houser *et al*. [45] showed the advantages in using photolithographic techniques for depositing thin electrodes with high manufacturing reliability and control, in comparison with tape electrodes that are cut and laid by hand and have thicknesses restricted to the ones commercially available. In order to enhance the lifetime of the actuator limiting the plasma damage of exposed SDBDPA electrodes, a surface coating of the W electrodes with sputtered TiN has been also performed. TiN is a well know wear resistant film widely adopted by the industry for coating of high speed steel tools and it was applied for the first time to SDBDPA electrodes by the authors of the current paper.

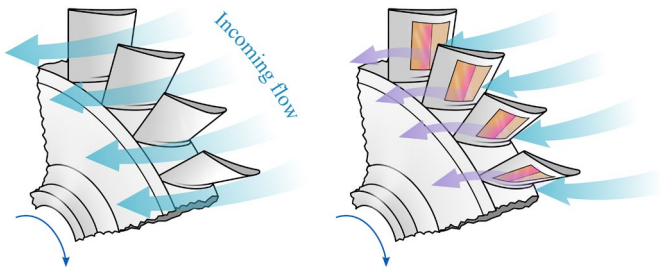

Figure 1: Conceptual drawing on SDBDPAs applied on the suction surface of LPT rotor blades: absence of control (left); presence of control (right).

3 Experimental procedure

3.1 Actuator fabrication

The manufacturing procedure, reported in Figure 2, was carried out at the National Research Council Institute for Microelectronics and Microsystems (CNR-IMM) in Lecce. The AF-32 glass samples were cleaned in acetone ultrasonic bath for 15 minutes and then rinsed in deionised water, followed by hotplate de-hydratation at 120°C for 300 seconds. The glass surface organic contaminants were removed by a 10 minutes oxygen plasma treatment at 1 Torr of absolute pressure (Figure 2a). A single layer of AZ 5214 reversal image photoresist was dispensed on the glass substrate and soft-baked at 110 °C for 40 seconds (Figure 2b). The patterning of the front (exposed) and backside (grounded) metal layers was realized by the lift-off technique and 365 nm optical lithography process. The photoresist layer was exposed to ultraviolet (UV) light (Figure 2c); after reversal image procedure completion, the sample was dipped into AZ 326 developer bath to remove soluble photoresist areas (Figure 2d). Samples were loaded into a direct current (DC) sputtering tool for deposition of 200 nm of W on the front side and 400 nm on the backside of the samples. A 10 nm thick adhesion layer of Ti was deposited on glass before than W deposition (Figure 2e). Finally, acetone was used to lift-off the metal and the photoresist onto the unmasked areas (Figure 2f). The same photolithographic and deposition procedure was repeated for the deposition of the TiN protective coating on the electrodes (Figure 2g-k). The deposition was carried out in a nitrogen/argon reactive gas mixture; the thickness of TiN onto previously deposited W electrode was 400 nm (with a 10 nm Ti adhesion layer). The TiN coating overlapped the tungsten electrode width by 200 microns on each side, in order to completely coat the sidewalls of electrode and increase the plasma resistance.

Figure 3 shows the actuator geometrical details and dimensions. The cross sectional view, with the representation of the deposition layers and their thicknesses, is reported in Figure 3 (a). A top view of the SDBDPA is instead depicted in Figure 3 (b). A scanning

electron microscope (SEM) image is also reported in Figure 3 (b), where it is well evident the TiN coating overlapping over the W/TiN electrode edge (200 µm).
Both electrodes had a spanwise length (*l*) of 30.4 mm. When allocated on the curved wall plate for the separation control experiments, the actuator backside electrode (denoted as "grounded electrode" in Figure 3) and the AF-32 dielectric were flush mounted at the wall of the profile, whereas the upper electrode (denoted as "exposed electrode" in Figure 3) emerged from the surface and was exposed to the surrounding air flow.

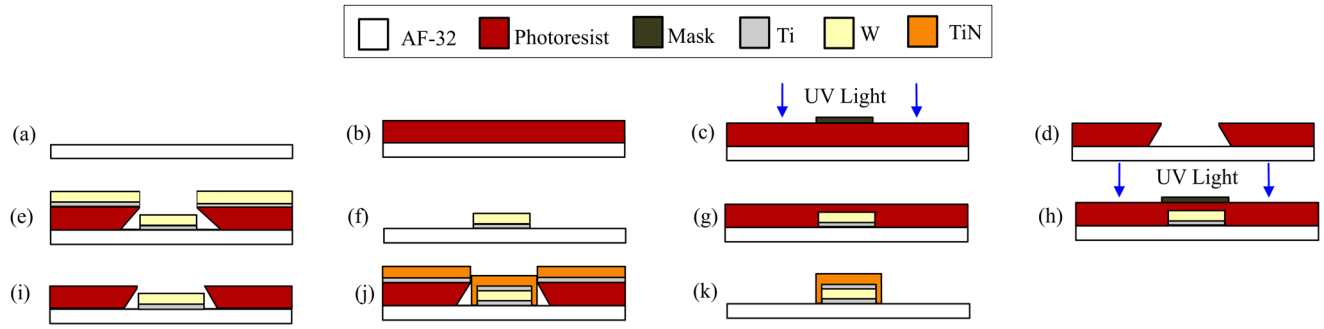

Figure 2. Actuator fabrication procedure by lift-off method.

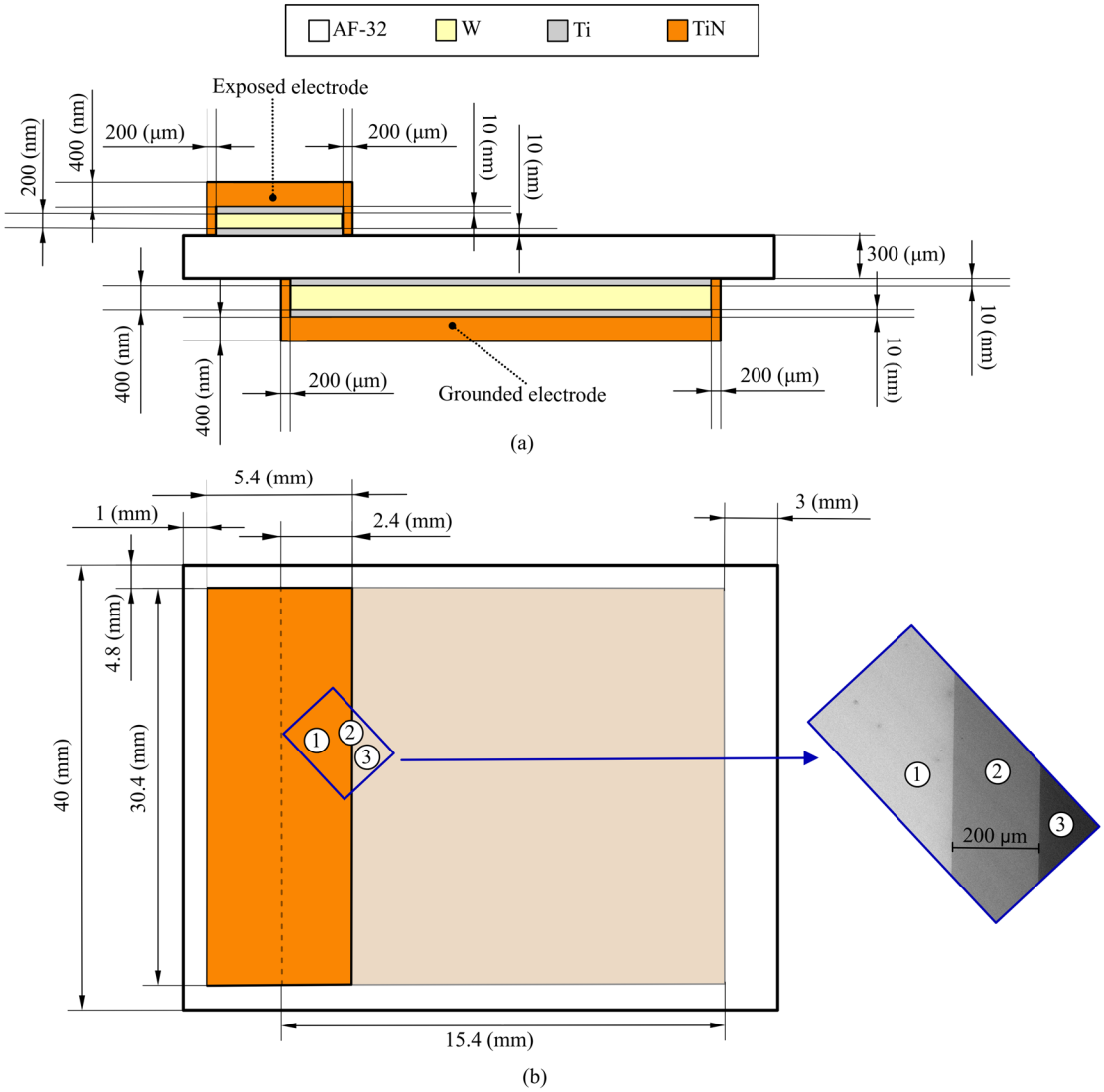

Figure 3. Actuator geometrical details and dimensions: (a) Cross sectional view; (b) Top view (a SEM image detail is also reported).

3.2 Actuator operation and measurements techniques

The flow field in presence and absence of actuation and the electrical properties of the SDBDPA were experimentally investigated in a closed loop wind tunnel with a 120 mm x 120 mm x 840 mm test section. All acquisitions were performed at

approximately 294 K and 1 bar. The SDBDPA was installed in a curved wall plate, designed to reproduce the separated flow on the suction surface of a turbine rotor blade [16]. The profile extended across all the wind tunnel test section spanwise (z -direction) length and it was characterized by a streamwise (x -direction) length c equal to 100 mm. An inlet guide wall was connected to the curved wall plate.

The profile design-surface velocity distribution was derived by Matsunuma and Segawa [1] from an inviscid calculation at the midspan of the blade of the turbine rotor installed in the annular turbine wind tunnel at the National Institute of Advanced Industrial Science and Technology [9], [42], [43]. The shape of the curved wall was designed using a simple one-dimensional continuity argument to match the design-surface velocity and pressure distribution of the corresponding turbine blade. Moreover, in order to avoid reflections of the laser beam that could affect the measurements (if occurring in proximity of the test area), the profile was manufactured in black color.

The wind tunnel had a centrifugal blower at the suction, which was driven by a frequency controller set to obtain a time averaged freestream velocity at the wind tunnel inlet (x =-86 mm) $v_{x,\infty}^{in}$ equal to 3 m/s. The $v_{\infty,x}^{in}$ values together with their turbulence level were accurately measured by LDV, due to the high sample size (500000 samples) high spatial (up to 0.05 mm) and temporal (up to 11.5 kHz) resolution [49], [50]. The 2-D inlet free-stream turbulence intensity Tu_{∞}^{in} was calculated by:

$$Tu_{\infty}^{in}\,(\%) = 100 \cdot \sqrt{\frac{1}{2}\left[\left(v'^{in}_{\infty,x}\Big|_{rms}\right)^2 + \left(v'^{in}_{\infty,y}\Big|_{rms}\right)^2\right]} \tag{1}$$

where $v'^{in}_{\infty,x}\Big|_{rms}$ and $v'^{in}_{\infty,y}\Big|_{rms}$ are the root-mean-square of the $v_{\infty,x}^{in}$ and the $v_{\infty,y}^{in}$ velocity fluctuations, respectively. A Tu_{∞}^{in} value around 1% was found. It is worth to mention that the y component $v_{\infty,y}^{in}$ of the freestream velocity was found to be two orders of magnitude smaller than $v_{\infty,x}^{in}$ and therefore v_{∞}^{in} was approximately equal to $v_{\infty,x}^{in}$. The Reynolds number (Re) based on the $v_{\infty,x}^{in}$ and c values was $2{\cdot}10^4$. The Re and turbulence intensity values here tested were approximately the same of the one investigated in Wang et al. [8] and Matsunuma et al. [3], [9].

Figure 4(left) shows the curved wall plate with the SDBDPA allocated, along with the adopted $x-y$ Cartesian coordinate system. A magnified view of the SDBDPA geometry is also depicted. The origin of the x-coordinate corresponds to the minimum passage area x-location and, for each x-coordinate, the origin of the y positions follows the curved wall plate. Figure 4 (right) shows instead a photograph of the experimental setup. The plasma actuator was placed in a groove made in the middle of the curved wall plate, at the front of the adverse pressure gradient region (deceleration/separation region) [15]. In particular, a 1 mm dielectric rim was left before the starting of the exposed electrode (see Figure 3 right), in order to avoid unwanted arching between the exposed and grounded electrode. Therefore, the actuator glass layer began at x=0, while the starting edge (left side edge) of the exposed electrode was located at x=1 mm.

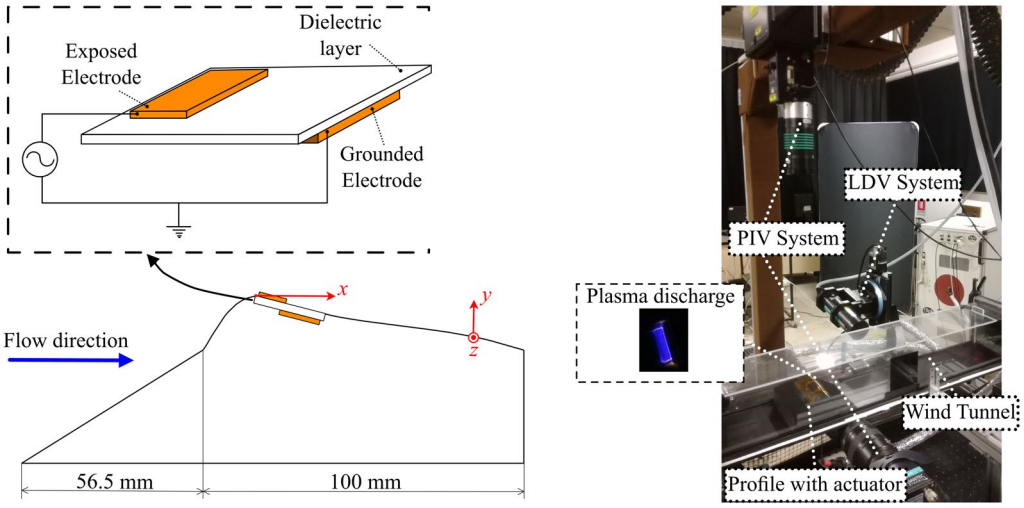

Figure 4. Curved wall plate, reference system and actuator details (left); Photograph of experimental setup and instrumentations (right).

The SDBDPA was powered with different HV waveforms (sinus, square and triangle), generated from a function generator (Enertec Schlumberger 4431) and then amplified to HVs with a Trek Model 40/15 amplifier. Each voltage waveform was characterized by different peak-to-peak voltages $\hat{\phi}_{pp}$, whereas the frequency $\hat{f}$ was fixed at 2 kHz. An acquisition/driving card (*NI-USB 6343*) was used to externally trigger the HV amplifier. The actuator exposed electrode was connected to the output of the HV

amplifier. The grounded electrode was instead connected to the ground. A sketch of the actuator electrical connections is reported in Figure 5.

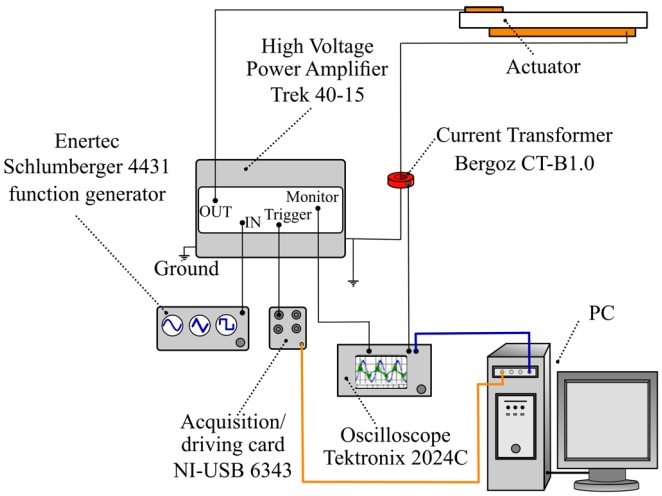

Figure 5. Sketch of the SDBDPA electrical connections and instrumentations for the power dissipation evaluation.

The applied voltage was measured with the voltage output monitor built into the amplifier. The current was instead measured by a current transformer (Bergoz Current Transformer CT-B1.0) placed in series between the grounded electrode and the ground. Both the amplifier voltage output monitor and the current transformer connector terminals were connected to an oscilloscope (Tektronix TDS2024C) and the respective signals were recorded. This allowed to retrieve the voltage-current characteristic curves (as a function of time, *t*).

2-D measurements of the flow velocities in presence of external flow and for both the "actuator ON" and "actuator OFF" conditions were performed. A streamwise plane ($x-y$) in proximity of the SDBDPA was investigated. In particular, PIV was used for both the actuator ON and actuator OFF test cases, while LDV only for the actuator OFF test cases. In the "actuator ON" conditions, simultaneously to each velocity measurement, the SDBDPA power dissipation was also evaluated (see paragraph 3.3).

In both the velocity measurement techniques, the seeding was generated by a *Magnum 850* smoke generator (particle size of 1-1.5 μm and particle density at room temperature of 0.95 kg/m^3). The Stokes number *St* resulted of the order 10^{-6}, indicating a good fluidic response from the tracer particles [33], [34]. The smoke was injected in a settling chamber, connected to the wind tunnel loop through a tube, from which it was sucked. Before each velocity measurement, new particles were added through the *Magnum 850* remote control, they were let circulating in the tunnel for about one minute and, just after, the acquisition was started. The blower was always kept on at constant rotating regime, i.e. it was never switched off between one velocity measurement and the other one.

In the PIV measurements a double pulse Nd: YAG laser, EverGreen (70-200 mJ @ 532 nm), was used to generate a light sheet (~1 mm thick) at the midspan section of the curved wall plate. A FlowSense EO camera 4M with a 2048×2048 resolution was used to acquire the PIV images, spanning from x=-5 mm to x=53 mm (see Figure 4 for the x zero position). It was equipped with a Nikkor 60 mm f/2.8 d A/F objective (set at an aperture of 4) and an interference filter (wavelength=532 nm) to eliminate the influence of the ambient light on the recorded images. The camera was operated in double-frame mode and 1000 image pairs per run were recorded at a repetition rate of 10 Hz.

Digital analysis was made using the Dantec DynamicStudio v4.10.67 software. In order to achieve the best possible accuracy in the PIV results, a mask was applied in the image area corresponding to the curved wall plate section and the noise contributions from the background were removed by subtracting the mean of the images [33]. The masked region was unwanted as it could produce bad vectors due to presence of the wall. An automatic and adaptive analysis method ("Adaptive PIV"), developed in the DynamicStudio software [51], [52], was used for calculating velocity vectors based on particle images. Peak validation/substitution was enabled during the cross-correlation processing [16], [33], [34]. Rectangular interrogation areas (IAs) with a maximum size of 64x64 pixels, minimum size of 32x32 pixels and grid step size (number of pixels from one IA to its neighbour) equal to 16 pixels were chosen. The spatial resolution of the processed PIV results was 0.5 mm. The mean velocity field was obtained by averaging the instantaneous PIV velocity maps of valid vectors, after than a vector masking was applied on them [53]. It was verified that the number N of samples for averaging was sufficient [36] to reach a steady value both in mean and root-mean-square (*rms*), as reported in Figure 6. In particular, eight random positions in the field of view, represented in Figure 6 (a), were selected. The time-averaged velocity *x*-component (v_x), the *rms* of the v_x velocity fluctuations ($v'_x|_{rms}$), the *rms* of the v_y velocity fluctuations ($v'_y|_{rms}$) and the v_x statistical percent error (ξ_{v_x}) of the velocity point samples were used for the statistical accuracy check of the PIV data.

The statistical percent error in the measurements of the mean velocity component v_x, ξ_{v_x}, was calculated from [34]:

$$\xi_{v_x} = 100\frac{1}{v_x}\left(\frac{t_{N-1,95\%}\, v'_x\big|_{rms}}{\sqrt{N}}\right) \tag{2}$$

where $t_{N-1,95\%}$ is the t estimator ($N-1$ degrees of freedom, 95% confidence interval).

As it is evident from Figure 6, the mean of the velocity and the *rms* of the velocity fluctuations tended to converge after the averaging of about 400 valid vectors, with an error ξ_{v_x} generally below 5%. The point P7 exhibited a higher error since it was located at the boundary line between the main flow and the separated flow. It was in fact characterized by high turbulence level (see Section 4).

The LDV experimental setup consisted of a FlowLite 2D (high Power) 2.2 mm 532/561 laser, a two-component Transmitter/Receiving Probe, equipped with a lens having 160.4 mm focal length, a Fiber PDA Detector Unit and a Flow Processor BSA P60. The probe was moved by motorized micrometer positioning stages. The measurements were performed in the same plane as the PIV measurements. LDV data analysis was performed using the Dantec BSA Flow Software v.5.02, taking 500.000 particles into account or 120 seconds of acquisition time when the seeding level was low (as it occurred near the wall location). The LDV measurements allowed achieving an accurate estimation of the velocity values and they were essentially used to validate the PIV data.

The uncertainty on the measured x and y position in the PIV vector fields, estimated by the guidelines reported by Raffel *et al.* [54], was about ±0.5 mm. For the LDV system it was instead of ±0.005 mm. The uncertainty in the time-averaged velocity measurements was estimated according to Moffat [55]. The statistical percent error in the estimation of the maximum value of the v_x velocity (Eq. 2) resulted in at worst 0.5% for the PIV measurements and 0.02% for the LDV ones. The statistical percent error in the minimum value of v_x resulted instead in at worst 6% for the PIV measurements and 0.6% for the LDV ones.

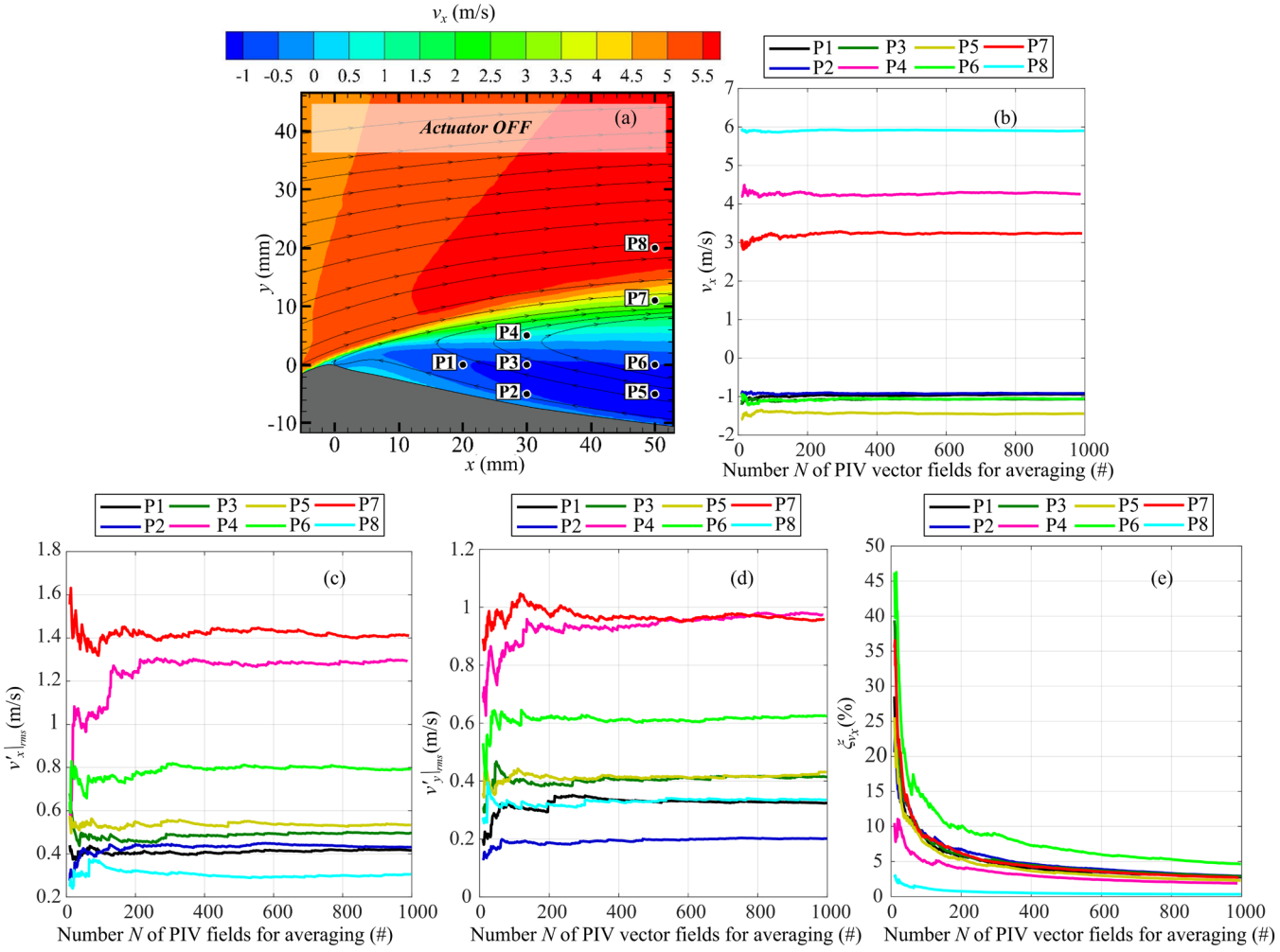

Figure 6: Example of the statistical analysis on PIV measurements: (a) map of the selected sampling points; convergence for increasing number of vector fields of: (b) v_x, (c) $v'_x|_{rms}$, (d) $v'_y|_{rms}$, (e) ξ_{v_x}.

3.3 Actuator performance indicators

The SDBDPA voltage-current characteristic curves, recorded during each PIV measurement test with actuator ON, were used for the actuator power dissipation calculation. The following procedure was adopted.

A single acquisition of the oscilloscope captured 2500 data points at a sampling rate of 25 MHz. For each input voltage, 128 single acquisitions were recorded and averaged. The mean values of the applied voltage signal ($\phi(t)$) and of the current signal ($I(t)$) were thus obtained. In order to increase the measurement accuracy, for each test case, the $\phi(t)$ - $I(t)$ curves were saved $\hat{N}$ times throughout the duration of each PIV experiment. The mean value of the respective power dissipations was considered representative of each test case. This procedure allowed also evaluating the actuator power consumption stability at given excitation conditions, ensuring that the actuator control authority was not changing during the respective velocity measurement. At fixed excitation conditions, the standard deviation between the individual power consumption measurements was at worst 0.2 W. It has to be noticed that only the data corresponding to one time period ($\hat{T}$) were selected for the electric power dissipation calculation. This was made through an in-house algorithm implemented in Matlab, which found the time instants corresponding to two consecutive maximum values of $\phi(t)$ and cut $I(t)$ and $\phi(t)$ acquired signals lying outside that time interval. In definitive, the electric power dissipation $\overline{P}$ was calculated as follows:

$$\overline{P} = \frac{1}{\hat{N}} \sum_{1}^{N} \left(\frac{1}{\hat{T}} \int_0^{\hat{T}} I(t)\phi(t) dt \right) \tag{3}$$

The numerical integration was performed using the trapezoidal rule and the uncertainty of each $\overline{P}$ value was estimated by standard uncertainty analysis methodology [55], resulting in at worst ±7% (see Table 2).

Aiming to correlate the relative jet momentum input by the actuators to the flow momentum, the PIV data were used for retrieving the 2-D momentum coefficient c_μ by [15]:

$$c_\mu = J \Big/ \tfrac{1}{2} \rho (v_{\infty,x}^{in})^2 c \tag{4}$$

where ρ is the fluid density and J is the steady wall-jet momentum produced immediately downstream of the actuator (x=20 mm is considered) , which was quantified by:

$$J = \int_{y_W}^{y_\infty} \rho (v_{x,on}^2 - v_{x,off}^2) dy \tag{5}$$

where, for a given x-coordinate, $v_{x,on}$ and $v_{x,off}$ are the time-averaged x-velocity profiles with and without plasma actuation. The y_W and y_∞ values are the y-coordinates of the profile wall and of the maximum height that we could resolve with the PIV acquisitions, respectively.

The obtained c_μ coefficients, together with the $\overline{P}$ values corresponding to the respective actuated conditions, allowed the definition of the c_μ coefficient "effectiveness", defined as c_μ / P. This parameter was very useful to assess the actuator performance.

Moreover, the PIV data were also used not only to retrieve the average velocity fields, but also determine the 2-D turbulence intensity Tu in the adverse pressure gradient region. According to [1], [15], [56], the Tu at each measurement point was calculated by:

$$Tu\ (\%) = 100 \cdot \frac{\sqrt{\frac{1}{2}\left[\left(v_x' \big|_{rms} \right)^2 + \left(v_y' \big|_{rms} \right)^2 \right]}}{v_{\infty,x}^{in}} \tag{6}$$

The v_x velocity and Tu maps in presence and absence of actuation allowed assessing the actuator effect on mean and unsteady quantities.

3.4 Test cases

Table 1 reports all the studied test cases, with indication of the test conditions and of the electrical power dissipation of each test case with actuator ON. The root-mean-square voltage $\hat{\phi}_{rms}$ values have been obtained by:

$$\hat{\phi}_{rms} = \frac{1}{\hat{T}} \int_0^{\hat{T}} (\phi(t))^2 dt \tag{7}$$

Figure 7 shows an example of the three actuation waveforms $\phi(t)$ and the corresponding current $I(t)$ flowing in the circuit, at similar applied peak-to-peak voltage $\hat{\phi}_{pp}$ and same frequency.

Test case	Actuator state	Waveform type	$\hat{\phi}_{pp}$ (kV)	$\hat{\phi}_{rms}$
A	OFF	-	-	
1B	ON	sinus	11.9±0.3	4.2±0.2
2B	ON	sinus	14.7±0.3	5.2±0.2
3B	ON	sinus	16.9±0.4	6±0.2
1C	ON	square	11.8±0.2	5.3±0.1
2C	ON	square	14.9±0.3	6.3±0.2
3C	ON	square	17.0±0.3	6.9±0.2
1D	ON	triangle	11.7±0.2	3.4±0.2
2D	ON	triangle	14.5±0.3	4.3±0.2
3D	ON	triangle	16.7±0.4	5.0±0.2

Table 1: Test cases ($v_{\infty,x}^{in}$ = 3 m/s, *Re* =2·10⁴, $\hat{f}$ =2 kHz).

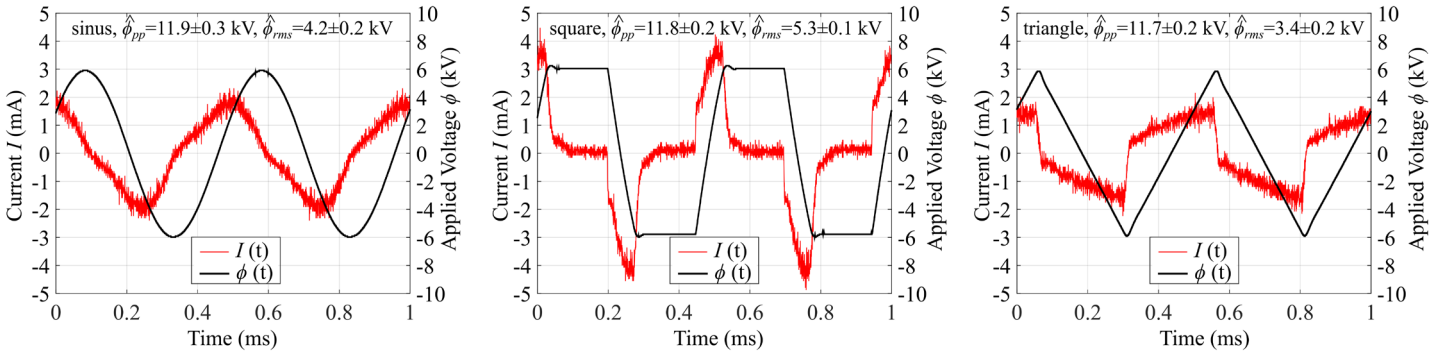

Figure 7: Voltage-current characteristic curves for the test cases 1B (left), 1C (middle) and 1D (right).

4 Results and Discussions

Figure 8 shows the vertical profiles of the v_x velocity for the test case A, taken over the profile at x = 0, 10, 20 and 30 mm with both the PIV and the LDV techniques. From the presented results separation certainly occurs in the adverse pressure gradient area along the curved wall and a reverse flow is present in the separation region. Considering the better accuracy of the LDV technique (see the paragraph 3.2), the good agreement between the PIV and LDV techniques allowed validating the PIV velocity measurements. As a consequence, only PIV was employed for the actuator ON test cases, later showed. In that way, the whole velocity field could be retrieved reducing the acquisition time while keeping a good accuracy.

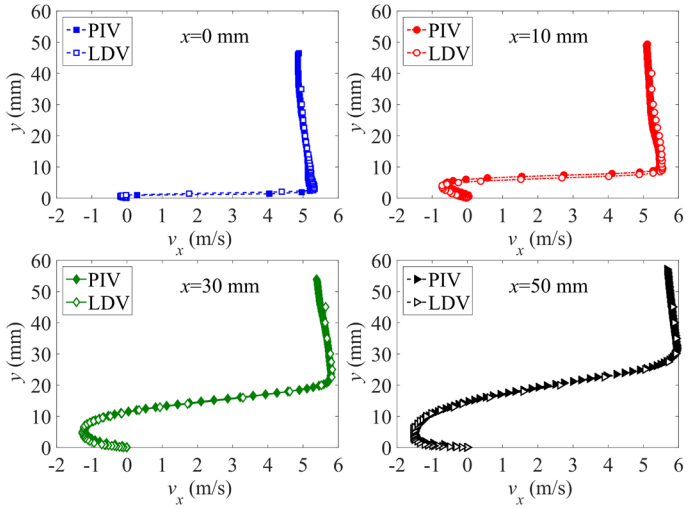

Figure 8. PIV and LDV velocity profiles comparison for the test case A (Actuator OFF).

Considering the actuator ON test cases, Table 2 reports their power dissipation, the c_μ coefficient and the $c_\mu / \overline{P}$ parameter. It provides a first comparison of the different actuation conditions.

The c_μ coefficient behaviour shows clearly that its value increased with the applied voltage, as the actuation effect became higher. At the same time, the electrical power dissipation raised too. However, when rising the voltage, the actuator effectiveness $c_\mu / \overline{P}$ parameter exhibited first an increase followed by a reduction when the highest voltage was applied. This occurred because the augmentation in power dissipation became higher than the one in c_μ coefficient.

Moreover, the sinus actuation had the highest c_μ and $c_\mu / \overline{P}$ values; their lowest values were given by the square one. Looking in fact at the power dissipations values, it evinced that at comparable peak-to-peak voltages, the sinus and triangle waveforms had similar power dissipations, while the square wave always implied higher $\overline{P}$ values. The square wave was characterized by the highest power dissipation, because of the high current peaks [38] (Figure 7).

Comparing instead the $\hat{\phi}_{rms}$ voltage values of the sinus and triangle waveforms, it could be noticed that, at comparable $\hat{\phi}_{rms}$ values, the test case 1B actuated less than the test case 2D, which in turn had higher dissipation value. It was confirmed by the test cases 2B and 3D results. A similar behaviour could be noticed by comparing the square wave with the triangle one (test cases 1C-3D). Considering now the sinus and the square waves, it evinced that at a similar $\hat{\phi}_{rms}$ value (test cases 2B-1C and test cases 3B and 2C) the sinus had higher actuation effect together with higher $\overline{P}$ values.

Test case	c_μ	$\overline{P}$ (W)	$c_\mu / \overline{P}$
A		-	
1B	0.0952±0.0006	1.47±0.04	0.065±0.002
2B	0.2165±0.0006	2.9±0.2	0.075±0.006
3B	0.268±0.002	4.7±0.2	0.057±0.003
1C	0.0730±0.0005	2.08±0.05	0.0351±0.0009
2C	0.1827±0.0006	3.7±0.2	0.049±0.003
3C	0.224±0.002	5.9±0.2	0.038±0.002
1D	0.0736±0.0006	1.38±0.04	0.053±0.002
2D	0.2005±0.0006	2.7±0.2	0.074±0.006
3D	0.230±0.001	4.5±0.2	0.051±0.003

Table 2: Test cases performances comparison (test case A: actuator OFF; test cases B, C, D: actuated by sinus, square and triangle, respectively; 1, 2,3: increasing $\hat{\phi}_{pp}$ applied voltage, respectively).

Figure 9 reports a comparison of the v_x velocity fields retrieved by PIV for all the test cases. In each iso-contour the streamlines of the velocity field are also superimposed upon the velocity distributions. It is evident that, when actuation was not present, separation was occurring in all the adverse pressure gradient area along the curved wall. When the actuator was switched on, the plasma generated a wall-jet [35], which brought to a local acceleration of the fluid downstream in the x direction. Therefore, in presence of actuation, the extension of the flow separation region was reduced and the magnitude of the negative velocity decreased. The higher was the applied voltage (i.e. higher power dissipations), the larger these reductions were. Moreover, the streamline paths show that the wall normal velocity component decreased and, therefore, the flow angle in both the main flow and in the boundary layer was reduced by the SDBDPA. In particular, the flow became more streamwise oriented in the main flow region and it was more attached and closer to the curved wall surface in the boundary layer [15], [16]. This effect was slightly enhanced in the sinus actuation test cases. The boundary layer modification could be explained by two consequences of the plasma actuation. The first one is the boundary layer energization due to the momentum introduced directly by the plasma actuation through the flow acceleration. The second one is the mixing effect between the boundary layer flow and the streamwise flow with higher momentum, which also energized the boundary layer.

Comparing the different actuation waveforms, not a substantial difference could be noticed in terms of flow control effect. However, as showed by the c_μ values results, at similar applied voltage the sinus waveforms slightly outperformed the others waveform, as confirmed also by the highest reduction of the negative velocity values at $x \approx$ 30-40 mm. However, a small recirculation was still present in the separation zone, even if at the highest tested $\hat{\phi}_{pp}$ value. Therefore, an increase in the momentum added by the plasma wall jet would be necessary to totally suppress the separated flow. For a given SDBDPA geometrical configuration, positioning and excitation waveform, this could be reached by rising the device power consumption [27], [28], [33], [38]. Therefore, excitation parameters ($\hat{\phi}_{pp}$ and /or $\hat{f}$ values) slightly higher than the ones here tested could bring to a full reattachment of the flow.

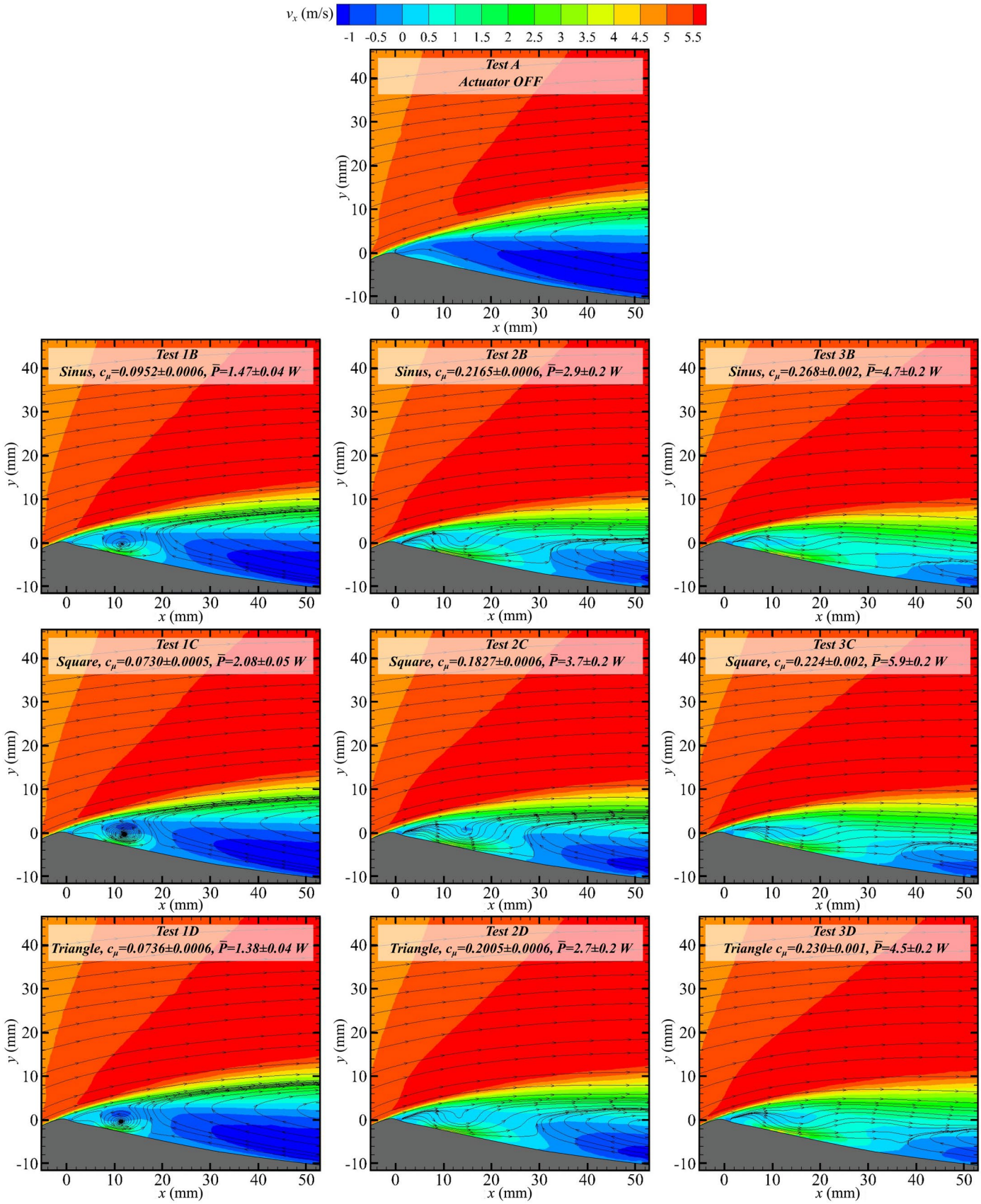

Figure 9: PIV v_x velocity iso-contours for the different test cases.

For a more quantitative evaluation of the actuation effect, Figure 10 reports the velocity profiles of the v_x velocity for the test case A (actuator OFF) and the test cases actuated with the sinus waveform. The region downstream the actuator is considered, in

particular the sections located at x = 20, 30 and 50 mm. It is evident that, except for the test case 1B where the actuation effect is almost negligible, the actuator operation led to a reduction of the boundary layer thickness and of the negative velocity values.

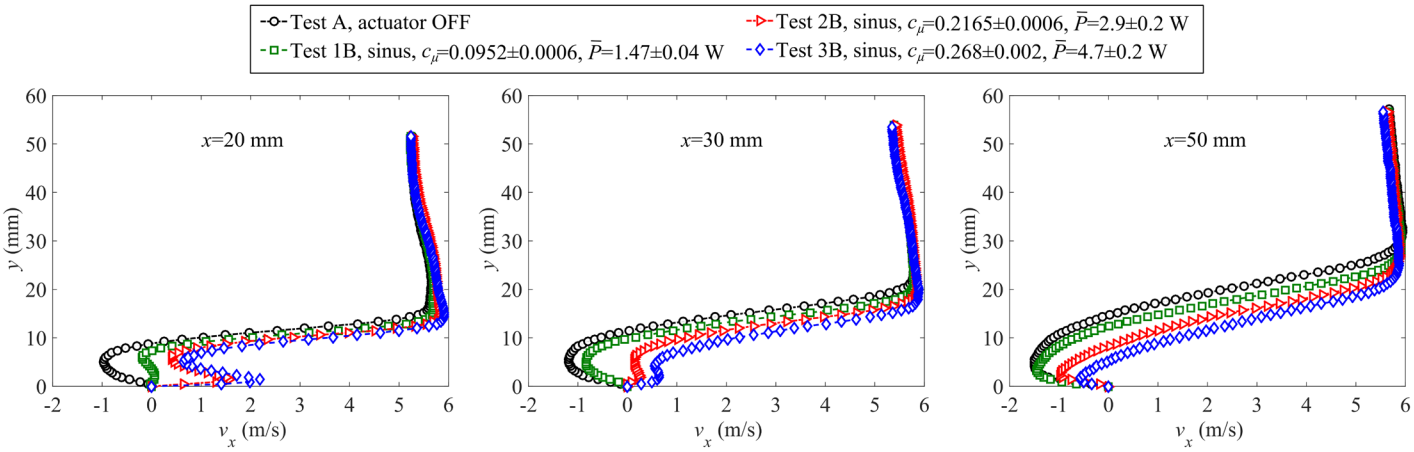

Figure 10: PIV *x*-velocity profiles taken at two different *x*-sections and for the actuator off case and the actuated cases with a sinus waveform.

The Tu contour maps for all the test conditions, calculated by using Eq. (6), are reported in Figure 11. In the not actuated test cases, a wide high turbulence region was present at the boundary line between the main flow and the separated flow, starting from x≈10 mm. A maximum Tu value of about 45% was reached. When the actuator was switched on, the high turbulence region moved further upstream and closer to the curved wall surface. This phenomenon was enhanced at higher excitation voltages, (i.e. higher boundary layer energization) and slightly higher Tu values were induced by the sinusoidal voltage excitation. This last result confirmed the observations of Bernard and Moreau [37], who found that the sinusoidal waveform enhanced the velocity fluctuations induced in an initially quiescent environment.

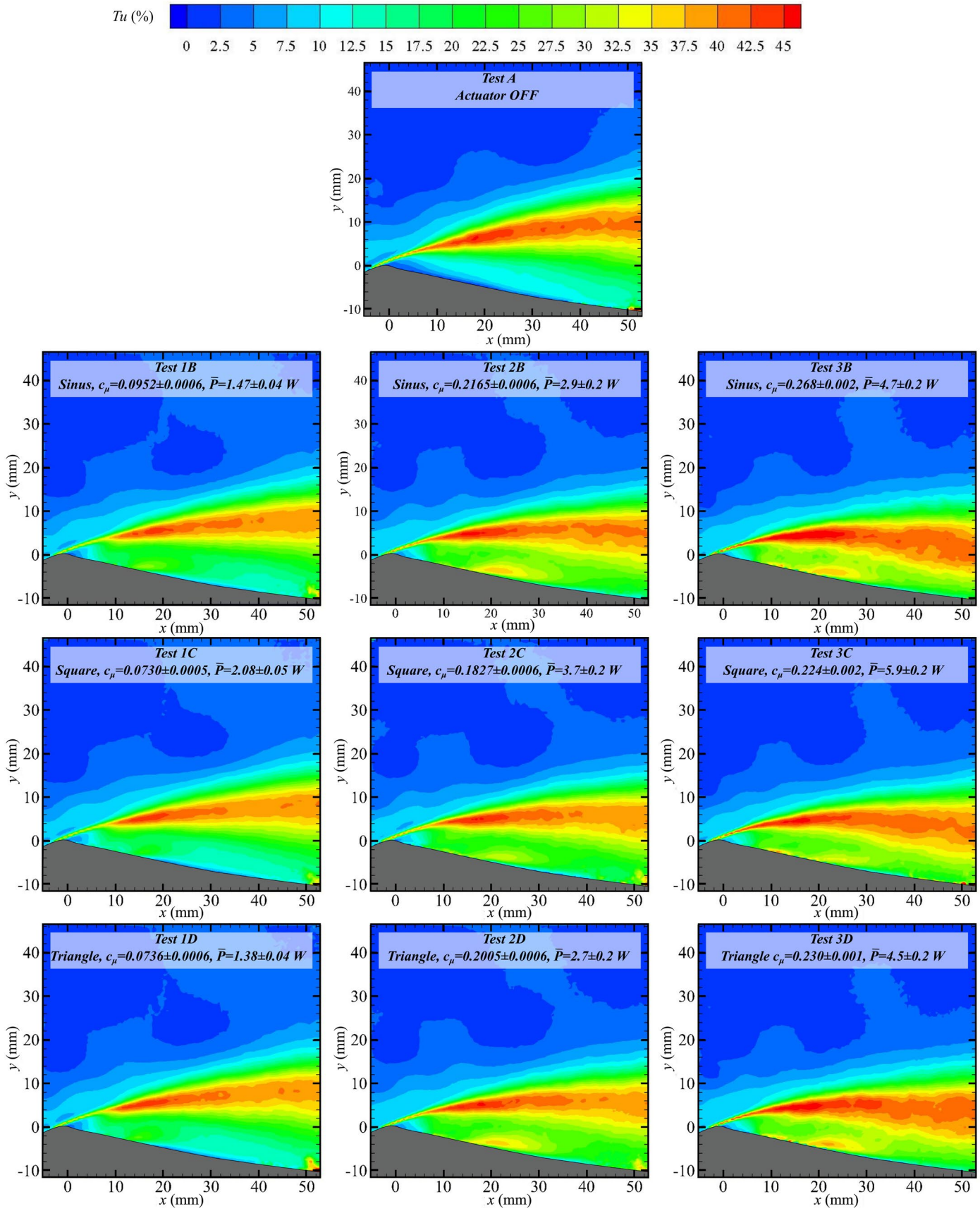

Figure 11: PIV turbulence intensity iso-contours for the different test cases.

5 Conclusions and Further Work

The present work investigated and compared experimentally the effect of the SDBDPA excitation voltage waveforms on flow separation control. A curved wall profile reproducing the suction surface of a LPT blade was taken as testing scenario. The plasma flow control effect was investigated at a *Re* number equal to $2 \cdot 10^4$ through both electrical and velocity measurements. Together with the voltage waveform type, also its amplitude was varied up to 17 kV peak-to-peak, while the applied voltage frequency was kept at 2 kHz.

The SDBDPA was fabricated by microfabrication techniques, involving metals thin film deposition and hard TiN coating for electrodes protection against plasma. Due to the possible device degradation in the plasma environment, an accurate materials selection was performed: Schott AF-32 glass as dielectric, while a multilayer TiN/W as electrode material.

Velocity data showed that when actuation was not present, separation was occurring in all the adverse pressure gradient area along the curved wall. Moreover, a wide high turbulence region was found at the boundary line between the main flow and the separated flow. Measurements in presence of actuation demonstrated that the SDBDPA operation brought to a decrease of the flow separation region extension, together with the magnitude of the negative velocity. Moreover, the flow angle in both the main flow and in the boundary layer was reduced by the active flow control effect; the flow became more streamwise oriented in the main flow region and more attached and closer to the curved wall surface in the boundary layer. Their reduction increased with the applied voltage (hand in hand with the power dissipation), as confirmed by the rise in the c_μ coefficient values, due to the higher actuation effect. However, for each waveform type the $c_\mu / \overline{P}$ parameter value first increased with the voltage, but after decreased when the highest voltage amplitude was applied. The latter was due to the higher rise in power dissipation with respect to the c_μ rise. The Tu results underlined that the actuator acted energizing the boundary layer as, when the actuator was switched on, the high turbulence region moved further upstream and closer to the curved wall surface.

Comparing the different HV excitation waveforms, it was found that, at comparable $\hat{\phi}_{pp}$ voltages, the sinus and triangle waveforms had similar power dissipation, while the square wave always implied higher $\overline{P}$ values. Considering instead the actuation effect, not a substantial difference was noticed between the different waveforms. However, the sinus voltage waveform always brought to a separation control effect slightly higher than the one of the other voltage waveforms, in terms of boundary layer thickness and negative velocities reduction in the separation region. However, a small recirculation was still present in the separation zone, even if at the highest tested $\hat{\phi}_{pp}$ value. At comparable $\hat{\phi}_{rms}$ applied voltage values, the sinus and square waveforms actuated less than the triangle one, which in turn had higher dissipation value. Considering instead the sinus and the square waves, the sinus had higher actuation effect together with higher $\overline{P}$ values. The evaluation of the c_μ and c_μ / P values confirmed that that the sinus had the highest performances, while their lowest values were given by the square wave actuation. Moreover, the Tu values were also slightly larger for the sinus actuation test cases, confirming that the sinusoidal waveform allows enhancing the velocity fluctuations.

In order to understand the limits of the tested actuator geometry in suppressing separation, the authors aim to perform further measurements at higher values for the actuator excitation parameters ($\hat{\phi}_{pp}$ and/or $\hat{f}$ values). The potentialities of employing the current actuator in a configuration with multiple SDBDPAs allocated in array, will be also investigated. This will show if it is possible to have the same or higher control authority (compared to a single device configuration) by reducing the total dissipated power.

Moreover, since no substantial difference in terms of control authority was noticed among the waveforms for the tested $\hat{\phi}_{pp}$ values and $\hat{f}$ =2 kHz, experiments will be performed with a varying $\hat{f}$ value and keeping the $\hat{\phi}_{pp}$ voltage constant. That study, together with the current paper results, will also demonstrate if it is more convenient to increase the actuation frequency instead than the applied voltage, in terms of dissipated power and flow control effect. In this context, unsteady (duty-cycle) actuation will be also investigated.

Finally, the device durability was here assessed only looking at the dissipated power stability during each velocity measurement. The authors aim to perform a deep investigation on electrodes and dielectric degradation through SEM images and EDS analysis on the new and used devices; the further work will then be the transfer of optimized W/TiN coated electrodes to a flexible substrate (Kapton) with a suitable deposited thick ceramic film to protect the exposed dielectric.

Acknowledgments

The authors kindly thank Dr. Maria Assunta Signore from the CNR-IMM for her contribution toward the actuator manufacturing.
This work is part of NATO AVT-254.

Nomenclature

c	length of the curved wall, m.
c_μ	steady 2-D momentum coefficient.
$\hat{f}$	applied voltage frequency, kHz.

$I(t)$ current signal, A or mA.
J steady 2-D wall jet momentum, Kg/s^2.
l electrode spanwise length, mm.
N number of valid vectors for the PIV data averaging.
$\hat{N}$ number of power measurements for the $\overline{P}$ averaging.
$\overline{P}$ electrical power dissipation, W.
Re Reynolds number based on the $v_{x,\infty}^{in}$ value and on the length c of the curved wall.
St Stokes number.
$\hat{T}$ time period, s.
t time instant, s.
$t_{N-1,95\%}$ t estimator ($N-1$ degrees of freedom, 95% confidence interval).
Tu turbulence intensity, %.
$\mathbf{v}$ velocity vector, m/s.
v_i time-averaged velocity i-component, m/s.
(x, y, z) Cartesian coordinate system, m.
λ wavelength, nm.
ξ_{v_x} v_x statistical percent error (%).
ρ fluid density, kg/m^3.
$\phi(t)$ applied voltage signal, V.
$\hat{\phi}_{rms}$ root-mean-square applied voltage, kV.
$\hat{\phi}_{pp}$ peak-to-peak applied voltage, kV.

Subscripts

on quantity evaluated with actuator on
off quantity evaluated with actuator off
rms root-mean-square
W profile wall.
x *x* Cartesian component.
y *y* Cartesian component.
∞ variable evaluated at the freestream.

Superscripts

in variable evaluated at the test section inlet (x=-86 mm)
′ fluctuation.

References

[1] T. Matsunuma and T. Segawa, “Effects of Input Voltage on Flow Separation Control for Low-Pressure Turbine at Low Reynolds Number by Plasma Actuators,” International Journal of Rotating Machinery, vol. 2012 (2012) 10 pages

[2] D. D. Sanders, W. F. O’Brien, R. Sondergaard, M. D. Polanka, and D. C. Rabe, “Predicting Separation and Transitional Flow in Turbine Blades at Low Reynolds Numbers—Part I: Development of Prediction Methodology,” J. Turbomach., vol. 133, no. 3 (2011) p. 031011.

[3] T. Matsunuma, “Unsteady Flow Field of an Axial-Flow Turbine Rotor at a Low Reynolds Number,” J. Turbomach., vol. 129, no. 2 (2006) 360–371.

[4] J. P. Bons, R. Sondergaard, and R. B. Rivir, “The Fluid Dynamics of LPT Blade Separation Control Using Pulsed Jets,” J. Turbomach., vol. 124, no. 1 (2002) 77-85.

[5] J. Avinalexander, C. Sarojmala, M. Muthukumar, K. Kannamanimuthu, A. P. Haran, S. Soundaranayagam, “Low Reynolds Number Performance of Small Engine Turbine Blade,” 2nd International Conference on Innovative Research in Engineering and Technology (iCIRET2013), January 3-5, 2013.

[6] Dries Verstraete, P. Hendrick, V. Djanali, J. Ling, K. Wong, S. Armfield, “Micro propulsion activities at the University of Sydney,” Powermems 2010 Conference, 2010.

[7] G. Jims John Wessley and Swati Chauhan, “Investigation on Scaling of Gas Turbine Engines for Drone Propulsion,” Int. J. Eng. Technol. Manag. Appl. Sci., vol. 5, no. 6 (2017) 48–53.

[8] X. Wang, L. Liang, and S. Kang, “Numerical Simulations on Flow Separation Within an Axial Turbine at Very Low Reynolds Number,” ASME Paper No. GT2015-43108.

[9] T. Matsunuma and Y. Tsutsui, “LDV Measurements of Unsteady Flow in a Turbine Rotor,” AIAA Paper No. 2002-2742.
[10] O. P. Sharma and T. L. Butler, “Predictions of Endwall Losses and Secondary Flows in Axial Flow Turbine Cascades,” J. Turbomach., vol. 109, no. 2 (1987) 229-236.
[11] J. Huang, T. C. Corke, and F. O. Thomas, “Plasma Actuators for Separation Control of Low-Pressure Turbine Blades,” AIAA J., vol. 44, no. 1 (2006) 51-57.
[12] S. I. Benton, C. Bernardini, J. P. Bons, and R. Sondergaard, “Parametric Optimization of Unsteady End Wall Blowing on a Highly Loaded Low-Pressure Turbine,” J. Turbomach., vol. 136, no. 7 (2014) 071013.
[13] M. J. Bloxham and J. P. Bons, “Combined Blowing and Suction to Control Both Midspan and Endwall Losses in a Turbomachinery Passage,” ASME Paper No. GT2010-23552.
[14] M. G. De Giorgi, C. G. De Luca, A. Ficarella, and F. Marra, “Comparison between synthetic jets and continuous jets for active flow control: Application on a NACA 0015 and a compressor stator cascade,” Aerosp. Sci. Technol., vol. 43 (2015) 256–280.
[15] E. Pescini, F. Marra, M. G. De Giorgi, L. Francioso, and A. Ficarella, “Investigation of the boundary layer characteristics for assessing the DBD plasma actuator control of the separated flow at low Reynolds numbers,” Experimental Thermal Fluid Science, vol. 81 (2016) 482-498.
[16] E. Pescini, F. Marra, M. G. De De Giorgi, L. Francioso, and A. Ficarella, “Investigations of the Actuation Effect of a Single DBD Plasma Actuator for Flow Separation Control Under Simulated Low-Pressure Turbine Blade Conditions,” ASME Paper No. GT2016-57432.
[17] D. Burman, T. W. Simon, U. Kortshagen, and D. Ernie, “Separation Control Using Plasma Actuators: Steady Flow in Low Pressure Turbines,” ASME Paper No. GT2011-46807.
[18] D. P. Rizzetta and M. R. Visbal, “Numerical Investigation of Plasma-Based Flow Control for Transitional Highly-Loaded Low-Pressure Turbine,” AIAA J., vol. 45, no. 10 (2007) 2554–2564.
[19] D. S. Martínez, E. Pescini, M. G. De Giorgi, and A. Ficarella, “Plasma-based flow control for low-pressure turbines at low-Reynolds-number,” Aircraft Engineering and Aerospace Technology, Vol. 89, no. 5 (2017) 671-682.
[20] J. Kriegseis, S. Grundmann, and C. Tropea, “Airflow influence on the discharge performance of dielectric barrier discharge plasma actuators,” Phys. Plasmas, vol. 19, no. 7 (2012).
[21] R. Pereira, D. Ragni, and M. Kotsonis, “Effect of external flow velocity on momentum transfer of dielectric barrier discharge plasma actuators,” J. Appl. Phys., vol. 116, no. 10 (2014) 103301.
[22] R. Erfani, H. Zare-Behtash, and K. Kontis, “Influence of shock wave propagation on dielectric barrier discharge plasma actuator performance,” J. Phys. Appl. Phys., vol. 45, no. 22 (2012) 225201.
[23] E. Moreau, “Airflow control by non-thermal plasma actuators,” J. Phys. Appl. Phys., vol. 40, no. 3 (2007) 605–636.
[24] J. H. Mabe, F. T. Calkins, B. Wesley, R. Woszidlo, L. Taubert, and I. Wygnanski, “Single Dielectric Barrier Discharge Plasma Actuators for Improved Airfoil Performance,” J. Aircr., vol. 46, no. 3 (2009) 847–855.
[25] J. Little, M. Nishihara, I. Adamovich, and M. Samimy, “High-lift airfoil trailing edge separation control using a single dielectric barrier discharge plasma actuator,” Exp. Fluids, vol. 48, no. 3 (2010) 521–537.
[26] M. P. Patel et al., “Scaling Effects of an Aerodynamic Plasma Actuator,” J. Aircr., vol. 45, no. 1 (2008) 223–236.
[27] F. O. Thomas, T. C. Corke, M. Iqbal, A. Kozlov, D. Schatzman, and N. Dame, “Optimization of Dielectric Barrier Discharge Plasma Actuators for Active Aerodynamic Flow Control,” AIAA J., vol. 47, no. 9 (2009) 2169–2178.
[28] G. T. Æ. M. Cazalens et al., “Optimization of a dielectric barrier discharge actuator by stationary and non-stationary measurements of the induced flow velocity: application to airflow control,” Exp. Fluids, vol. 43, no. 6 (2007) 917–928.
[29] C. L. Enloe et al., “Mechanisms and Responses of a Dielectric Barrier Plasma Actuator: Geometric Effects,” AIAA J., vol. 42, no. 3 (2004) 595–604.
[30] R. Erfani, H. Zare-Behtash, C. Hale, and K. Kontis, “Development of DBD plasma actuators: The double encapsulated electrode,” Acta Astronaut., vol. 109 (2015) 132–143.
[31] R. Erfani, T. Erfani, S. V. Utyuzhnikov, and K. Kontis, “Optimisation of multiple encapsulated electrode plasma actuator,” Aerosp. Sci. Technol., vol. 26, no. 1 (2013) 120–127.
[32] R. Erfani, H. Zare-Behtash, and K. Kontis, “Plasma actuator: Influence of dielectric surface temperature,” Exp. Therm. Fluid Sci., vol. 42 (2012) 258–264.
[33] E. Pescini, L. Francioso, M. G. De Giorgi, and A. Ficarella, “Investigation of a Micro Dielectric Barrier Discharge Plasma Actuator for Regional Aircraft Active Flow Control,” IEEE Trans. Plasma Sci., vol. 43, no. 10 (2015) 3668–3680.
[34] E. Pescini, M. G. De Giorgi, L. Francioso, A. Sciolti, and A. Ficarella, “Effect of a micro dielectric barrier discharge plasma actuator on quiescent flow,” IET Sci. Meas. Technol., vol. 8, no. 3 (2014) 135–142.
[35] E. Pescini, D. S. Martínez, M. G. De Giorgi, and A. Ficarella, “Optimization of micro single dielectric barrier discharge plasma actuator models based on experimental velocity and body force fields,” Acta Astronaut., vol. 116 (2015) 318–332.
[36] R. Ruisi, H. Zare-Behtash, K. Kontis, and R. Erfani, “Active flow control over a backward-facing step using plasma actuation,” Acta Astronaut., vol. 126 (2016) 354–363.
[37] N. Benard and E. Moreau, “Role of the electric waveform supplying a dielectric barrier discharge plasma actuator,” Appl. Phys. Lett., vol. 100, no. 19 (2012) 193503.
[38] J. Jolibois and E. Moreau, “Enhancement of the electromechanical performances of a single dielectric barrier discharge actuator,” IEEE Trans. Dielectr. Electr. Insul., vol. 16, no. 3 (2009) 758–767.
[39] M. Kotsonis and S. Ghaemi, “Performance improvement of plasma actuators using asymmetric high voltage waveforms,” J. Phys. Appl. Phys., vol. 45, no. 4 (2012) 045204.

[40] D. F. Opaits et al., “Experimental investigation of dielectric barrier discharge plasma actuators driven by repetitive high-voltage nanosecond pulses with dc or low frequency sinusoidal bias,” J. Appl. Phys., vol. 104, no. 4 (2008) 043304.
[41] J. Huang, T. C. Corke, and F. O. Thomas, “Unsteady Plasma Actuators for Separation Control of Low-Pressure Turbine Blades,” AIAA J., vol. 44, no. 7 (2006) 1477–1487.
[42] T. Matsunuma, H. Abe, and Y. Tsutsui, “LDV Measurements of Unsteady Flow within a Turbine Rotor at Low Reynolds Numbers.,” JSME Int. J. Ser. B, vol. 45, no. 3 (2002) 457–464.
[43] T. Matsunuma and Y. Tsutsui, “Effects of Low Reynolds Number on Wake-Generated Unsteady Flow of an Axial-Flow Turbine Rotor,” Int. Jou. of Rotating Mac., (2005) 1–15.
[44] E. Pescini, M. G. De Giorgi, L. Francioso, A. Taurino, M. C. Martucci, and P. Lavoie, “Electrode Material Degradation Monitoring for Durable Dielectric Barrier Discharge Plasma Actuators Manufacturing,” 54th AIAA Aerospace Sciences Meeting, 2016.
[45] N. M. Houser, L. Gimeno, R. E. Hanson, T. Goldhawk, T. Simpson, and P. Lavoie, “Microfabrication of dielectric barrier discharge plasma actuators for flow control,” Sens. Actuators Phys., vol. 201 (2013) 101–104.
[46] J. Pons, L. Oukacine, E. Moreau, and J.-M. Tatibouet, “Observation of Dielectric Degradation After Surface Dielectric Barrier Discharge Operation in Air at Atmospheric Pressure,” IEEE Trans. Plasma Sci., vol. 36, no. 4 (2008) 1342–1343.
[47] A. R. H. Rigit, K. C. Lai, and D. B. L. Bong, “Degradation of a dielectric barrier discharge plasma actuator,” IEEE 9th Int. Conf. on the Prop. and App. of Die. Mat., (2009) 569–572.
[48] R. E. Hanson, N. M. Houser, and P. Lavoie, “Dielectric material degradation monitoring of dielectric barrier discharge plasma actuators,” J. Appl. Phys., vol. 115, no. 4 (2014) 043301.
[49] T. Saga, H. Hu, T. Kobayashi, S. Murata, K. Okamoto, and S. Nishio, “A comparative study of the PIV and LDV measurements on a self-induced sloshing flow,” Jou. of Visualization, vol. 3, no. 2 (2000) 145–156.
[50] G. P. Romano, “PIV and LDA velocity measurements near walls and in the wake of a delta wing,” Opt. Lasers Eng., vol. 16, no. 4–5 (1992) 293–309.
[51] C. J. Kähler et al., “Main results of the 4th International PIV Challenge,” Exp. in Fluids, vol. 57, no. 6 (2016).
[52] Dantec Dynamics A/S, DynamicStudio User’s Guide V4.10. 2014.
[53] F. Gökhan Ergin, “Dynamic Masking Techniques for Particle Image Velocimetry,” J Therm. Sci. Technol., vol. 37, no. 2 (2017) 61–74.
[54] M. Raffel, C. E. Willert, and J. Kompenhans, “Particle image velocimetry: a practical guide”, Springer, 1998.
[55] R. J. Moffat, “Describing the Uncertainties in Experimental Results,” Exp. Thermal and Fluid Sci., vol. 1, no. 1 (1988) 3–17.
[56] P. Mycek, B. Gaurier, G. Germain, G. Pinon, and E. Rivoalen, “Experimental study of the turbulence intensity effects on marine current turbines behaviour. Part I: One single turbine,” Renew. Energy, vol. 66 (2014) 729–746.